Azimuthal AVO over a simulated fractured physical model medium

Faranak Mahmoudian, Gary Margrave, and Joe Wong

ABSTRACT

We have verified the suitability of seismic data from a physical model for a quantitative amplitude analysis of anisotropic targets. Physical model data have often been used for traveltime analysis, while incorporating them in an amplitude analysis was limited due, in part, to the large size, highly-directional physical model transducers employed as sources and receivers. We acquired multi-offset, multi-azimuth, seismic data over a simulated fractured layer overlain by two isotropic layers with the most top layer being water. We simulated the fractured medium by constructing a physical layer, with horizontal transverse anisotropy (HTI), from phenolic material. Acquisition was designed to avoid the overlapping of the primary and ghost events. We treated the large-size transducers as seismic arrays and employed an array-type correction to compensate for their effects on seismic amplitudes. The PP reflection amplitudes from the top of the simulated fractured layer, after required AVO corrections, reveal a clear azimuthal variation caused by the simulated fractured layer and agreed with amplitudes predicted theoretically.

INTRODUCTION

Seismic modeling plays an important role in improving our understanding of seismic wave propagation and the verification of processing algorithms. Seismic modeling, the process through which a subsurface geologic model is transformed into a seismic record, has been extensively done using numerical methods. The mathematical formulation (acoustic or elastic) of wave propagation, and complexities in the computational process when modeling complex geological features, make numerical modeling challenging. Physical modeling, the alternative to numerical methods, has the advantage of changing real seismic wave propagation even for complex media.

Physical model data have been used for many years to simulate exploration targets, as in the example of a fractured medium. Traveltime and qualitative amplitude analysis of physical model data acquired over simulated fractured media have been employed by many researchers. A qualitative amplitude variation with offset and azimuth (AVAZ) analysis was conducted by Luo and Evan (2004) on physical model data acquired over a layer of compressed thin isotropic plexiglass plates, simulating regularly spaced vertical fractures in an isotropic background (a horizontally transverse isotropy (HTI) medium). Chang and Gardner (1997); Tadepalli (1995); Mah and Schmitt (2001a); Wang and Li (2003) used phenolic material which exhibits orthorhombic symmetry (Cheadle et al., 1991), as a simulated fractured medium, to investigate qualitatively the effects of vertical fractures on reflection data.

A next step for physical modeling to become more upstream is the verification of the suitability of physically modeled data in a quantitative amplitude analysis. therefore, the effect of large highly-directional physical model transducers on wavelet amplitude should be considered. The generated waveform and directional characteristic of the standard phys-

ical model circular transducer were examined by Buddensiek et al. (2009) and Bretaudeau et al. (2011). We present a verification of the suitability of physical model data for an amplitude analysis.

We acquired 3D marine multi-offset, multi-azimuth physical model seismic data over an LE-grade phenolic layer, simulating a fractured medium using the University of Calgary's seismic physical modeling facility. We quantitatively investigated the AVO behavior of the P-wave reflections from two isotropic/isotropic and isotropic/anisotropic interfaces which successfully agreed with the theoretical predictions. We corrected the reflection amplitudes using standard AVO corrections for marine data, and additionally, a directivity correction to compensate for the effects of the large physical model transducers.

PHYSICAL MODELING EXPERIMENT

In physical modeling, seismic wave propagation and recording are performed on a small-scale earth model. The scaling factor for our modeling system is 10000, so that a model dimension of 1mm represents 10m, and the dominant frequency of 500kHz represents 50Hz in the real world. Having the same scale for length and time, the actual velocity of the medium remains unscaled.

Our model consists of four layers, an anisotropic phenolic layer, and three isotropic layers (Figure 1). Some elastic properties of the modeling material are listed in Table 1. The phenolic LE^{TM} material we used is composed of laminated sheets of linen fabric bonded together with phenolic resin. Phenolic materials, because of their micro-layered texture, can be used to simulate finely layered structure rocks, such as sandstone, shale, or fractured limestone (Chang and Gardner, 1997).

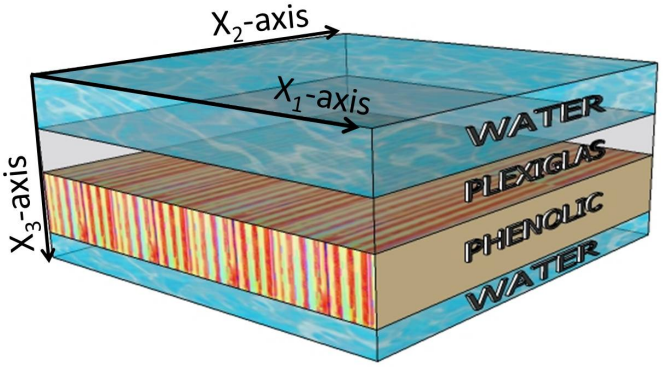

FIG. 1. The four-layered earth model used in physical modeling acquisition.

A manufactured board of phenolic material is milled to provide flat and perpendicular surfaces paralleling the layering, the warp, and the weave of linen fabric as closely as possible. Hence, the symmetry of phenolic materials is relatively well controlled (Mah and Schmitt, 2001b). To construct our simulated fractured layer, a board of phenolic material with horizontally laid linen fabric was cut into slabs along planes orthogonal to the plane of then linen layers. These were rotated 90° and bonded together with epoxy under a uniform high pressure. This constructed layer simulates a horizontal layer with vertical fractures at a single orientation.

	P-velocity (m/s)	S-velocity (m/s)	Density (g/cc)
Water	1485	~ 0.0	1.00
Plexiglas	2745	1380	1.19
Phenolic	3530 ($\|\|$) 2900 ($\perp$)	1700 ($\|\|$) 1520 ($\perp$)	1.39

Table 1. A summary of the physical properties of the materials.

Previous research on this constructed phenolic layer characterized it by estimating all its elastic constants using group velocity inversion (Mahmoudian et al., 2012), the constructed phenolic layer, although orthorhombic, closly resembles a HTI layer. Table 2 summarizes its estimated anisotropy parameters where $(\epsilon^{(V)}, \delta^{(V)}, \gamma)$ are the HTI parameters defined by Rüger (2001). We assume this constructed layer as a homogeneous solid which is clearly a scale dependent assumption, because sufficiently short wavelengths will respond to the heterogenous detail in our constructed layer. However, our results showed frequency dispersion to be minimal.

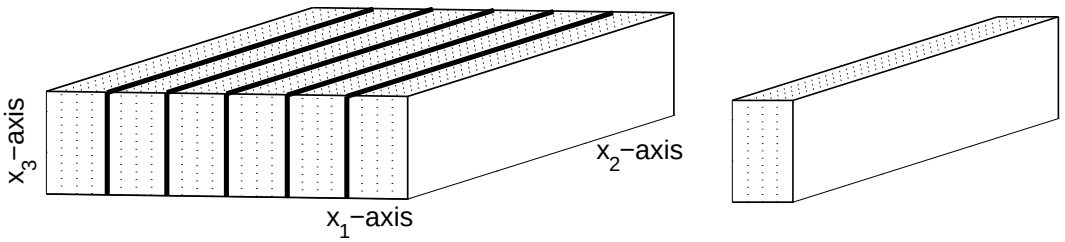

FIG. 2. (a) The simulated fractured layer with a scaled approximate area of 5700m$\times 5700$m and a thickness of 702m. (b) A slab of phenolic material, with dashed lines displaying the linen planes.

$\epsilon^{(V)}$	$\delta^{(V)}$	γ
$\frac{C_{11}-C_{33}}{2C_{33}}$	$\frac{(C_{11}+C_{55})^2-C_{33}+C_{55})^2}{2C_{33}(C_{33}-C_{55})}$	$\frac{C_{44}-C_{55}}{2C_{55}}$
-0.145	-0.185	0.117

Table 2. Anisotropy parameters of the simulated fractured layer.

Laboratory set-up

The plexiglass and simulated fractured layer were machined, to ensure flat and smooth surfaces, coated with a thin layer of epoxy glue, and compressed together under high pressure to ensure a welded contact. The two layers were submerged in a large water tank and located above the base water layer by adjustable screws fixed at the corners of the tank. We carefully leveled our model and made sure that the interfaces have no dip, by equating the reflection traveltimes from the upper interface at each corner, within the limits of our experimental recordings.

In physical modeling, the role of sources and receivers are played by ultrasonic piezoelectric transducers. A piezoelectric material has the property that, if deformed by external mechanical pressure, electric charges are produced on its surface (e.g, acting as a seismic receiver), and if placed in an electrical field, changes its form producing mechanical pressure (e.g, acting as a seismic source) (Krautkrämer and Krautkrämer, 1986). We used piezoelectric pin CA-1136 transducers with each piezoelectric element being 1.33mm in diameter. As receivers these transducers simulate vertical component geophones. These transducers produce an acoustic wavelength of ~ 2.8mm, corresponding to a wavelet with a center frequency of 520Hz for P-waves.

The modeling system is equipped with a robotic positioning system with two separate moving arms for positioning the source and receiver. Vertical stacking of repeated source excitations for each source-receiver position, and the progressive re-positioning of the source and receiver transducers, generate a multi-offset CMP seismic gather with high signal-to-noise ratio. The source pulse is highly repeatable over many hours of acquisition. The pulse excitation is provided by a high voltage pulse generator which has independent voltage control. We used sufficiently strong voltage (325 V) to image the reflection from the top of the fractured layer without clipping the first reflector amplitudes. Hence the bottom of the fractured layer was not recorded well as we would have liked (Figure 4). The robotic positioning system can accurately locate source and receivers to within 0.1mm. Once the initial source-receiver offset is set, the subsequent increments in offset are computer controlled and are accurately known. We manually positioned the first source and receiver locations according to a predefined coordinate system. With the large transducers, the effective first source-receiver distance is not automatic. To check the accuracy of the first source-receiver offset using the positions of the receivers, we fitted the fist-break traveltimes using least-squares; then we obtain the first source-receiver offset and the velocity of water (see appendix A). More details about laboratory equipment and set-up are as described by Wong et al. (2009).

Data acquisition

To collect the physical model reflection data, we used a common-midpoint (CMP) shooting arrangement similar to Chang and Gardner (1997). The seismic traces are gathered with respect to one CMP point for a range of offsets and azimuths. The acquisition coordinate system was chosen along the fracture system; the vertical is the x_3-axis, the x_1-axis runs along the symmetry axis, and the x_2-axis coincides with the fracture planes of the simulated fractured layer (Figure 3). A total of nine large-offset CMP seismic lines were recorded along azimuthal directions of $0°$, $14°$, $27°$, $37°$, $45°$, $53°$, $63°$, $76°$, and $90°$ with respect to the x_1-axis. Figure 3 shows the acquisition geometry. During data acquisition, elastic waves were emitted and received by a source-receiver pair starting with (S_1, R_1), collecting the first trace of each azimuth line. The source-receiver pair was then moved outwards to collect other traces of that azimuth. As the robotic positioning system was only able to make movements along the principal axis of x_1 and x_2, to acquire the azimuth lines the source and receiver were moved at $(\Delta x, \Delta y)$ intervals. The scaled $(\Delta x, \Delta y)$ intervals are $(50, 0)$, $(40, 10)$, $(40, 20)$, $(40, 30)$, $(40, 40)$, $(30, 40)$, $(20, 40)$, $(10, 40)$, and $(0, 50)$, corresponding to the nine azimuths respectively. The maximum scaled offset is 3400m,

mapping a CMP point at the top of the fractured layer at the scaled depth of 1200m. The scaled depth of overburden water, read from near-offset reflection data, is roughly 700m.

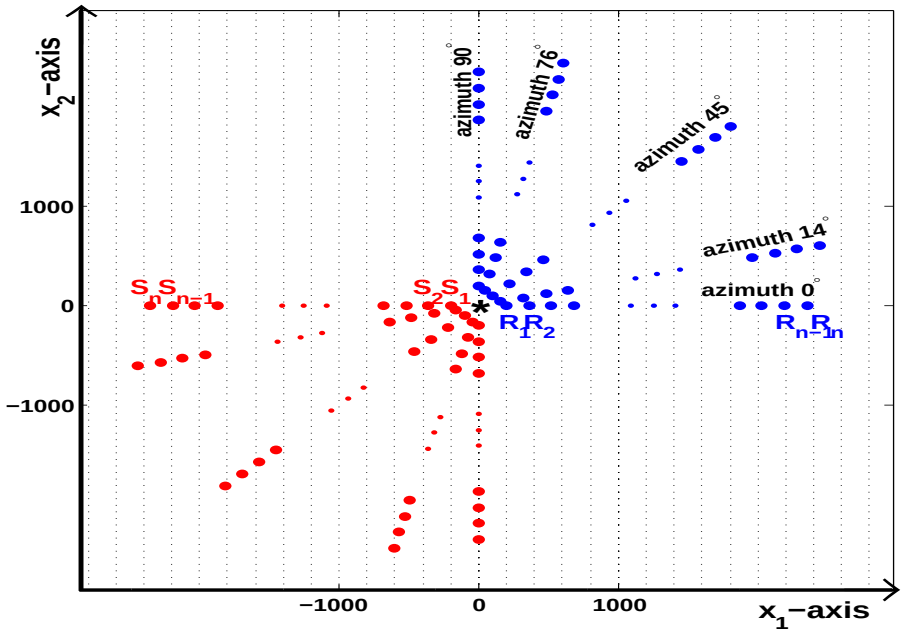

FIG. 3. A map view of the acquisition geometry of the CMP survey lines. The background thin lines schematically display the fracture strike direction with the line spacing not representative of the fracture density distribution. The azimuth angle of survey lines is with respect to the symmetry axis of the simulated fractured layer. The imaged CMP point is indicated by an $\star$. Receivers are shown in red and the sources are shown in blue. The x_1- and x_2-axis are showing the scaled dimensions in meters. Only five azimuth lines from a total of nine are displayed. The maximum number of traces in each azimuth line is 291. A total of 2499 traces was acquired in the CMP gather.

Figure 4 shows the CMP seismic line acquired along an azimuth of 0° (fractured symmetry axis) and 90° (fracture plane). Five events are recognizable from the reflection data. The three strong PP reflections from the plexiglass top (labeled "A"), fracture top (labeled "B") and base layer (labeled "E"), a strong PS reflection from the fracture top (labeled "C"), and a very weak PP reflection from bottom of the fractured layer (labeled "D"). The reflections from the plexiglas top and fractured top (labeled "A and "B"), appearing approximately at 0.9s and 1.2s, are examined in the amplitude analysis.

In our physical modeling experiment, as the sources and receivers operate near the water surface, primary and ghost reflections are expected. The overlapping of primary and ghost reflections corrupts the amplitude information required for an amplitude analysis, and therefore should be avoided. We decided to acquire the azimuth lines with the transducer's tip 2mm within the water, so that the primary and ghost events are separated. This decision is based on a preliminary experiment designed to examine the behavior of the ghosts. In this experiment, the source and receiver were kept at a fixed offset of 10mm, and seismograms were recorded at 0.2mm depth intervals as both transducers were raised from a depth of 10mm up to a depth of 0mm (at which the active tips of the transducers were nominally even with the water surface). Figure 5 shows a suite of seismograms from this experiment. For each reflector, three events are collected, a primary, a ghost, and a constant traveltime event. The primary has a time moveout towards earlier times as tip depth increases. This is as expected since, as tip depth increases, the lengths of the raypaths from the tips to

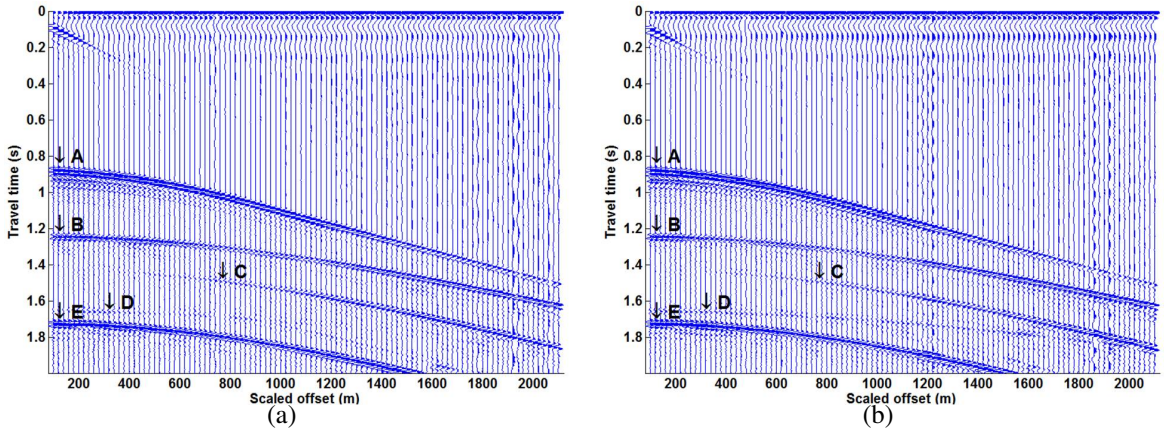

FIG. 4. (a) 0° azimuth data, (b) 90° azimuth data with a long gate automatic gain control applied. In the display,event "A" is the PP reflection from the top of the plexiglas layer, event "B" is the PP reflection from the top of the fractured layer (our target), event "C" is the PS reflection from the top of the fractured layer, event "D" is the PP reflection from the bottom of the fractured layer, and event "E" is the PP reflection from the base layer. Note that the PP reflection event from the bottom of the fractured layer (D) in 0° azimuth data, due to the higher amplitude decay along the fractures symmetry axis, is hardly visible.

the reflecting interface decreases (Figure 6(a)). For the ghost, the arrival times increase as tip depth increases. which is also expected (Figure 6(b)), since the total raypaths for this ghost includes segments from the tips to the surface (lengths increase with tip depth) and segments from the surface to the reflecting interface (lengths are independent of tip depth). The third event has an almost constant traveltime, and has a traveltime as if the source and receiver were both located at the water surface, and therefore there is no apparent change in travel path length as tip depth changes. This constant traveltime event is generated by two single-leg ghost events at the source or receiver (Figure 6(c)). The existence of two single-leg ghosts makes the constant traveltime event appear strong. In appendix B, we prove that the single-leg ghost event has a constant traveltime as if the wave was generated at water contact with the source transducer, reflected from the CMP point between the source and receiver, and recorded at water contact with the receiver transducer. The optimum transducers tip depth within the water was chosen to be $2mm$, as it is the minimum transducer tip depth at which the primary and ghosts events can be recorded without any overlap. A larger transducer tip depth is not desired as the ghost events from the upper reflector leak into the lower reflectors.

Amplitude picking

For each azimuth line, the P-wave reflection from the reflecting interfaces of interest were identified, and the arrival times and reflection amplitudes were picked from raw data using an automatic picker available in the CREWES MatLab library. For the plexiglas top, the amplitudes were picked on the primary event which follow the arrival times strong and clear. For the fracture top, as the primary event was weak and hard to pick, the amplitudes were picked on the strongest wavelet following each arrival time, associated with the single-leg ghost event.

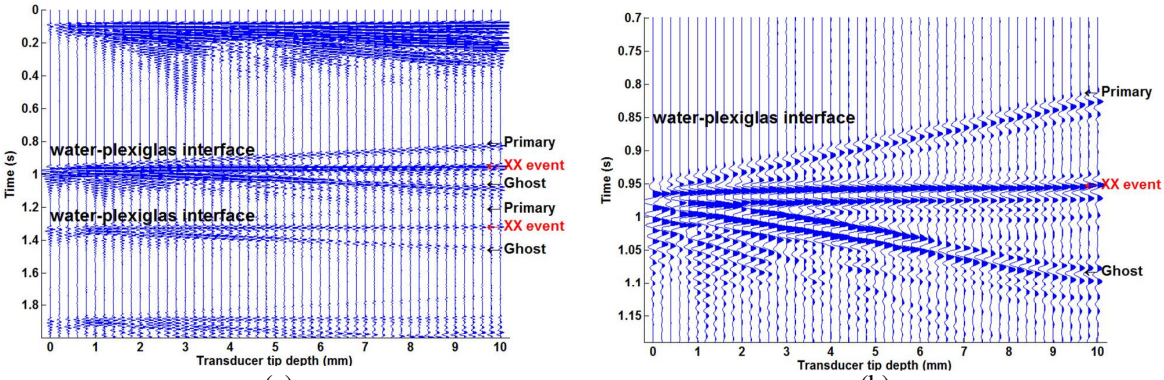

FIG. 5. (a) Data acquired at a single source-receiver offset of 10mm with different transducer depths in water. b) Expanded time scale to show detail of the reflections from the top of the plexiglas.

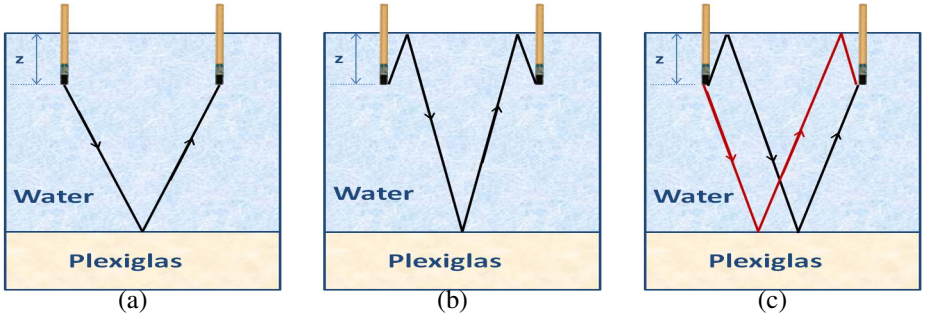

FIG. 6. (a) Primary raypath. (b) Ghost raypath. (c) Asymmetric raypaths, two single-leg source and receiver ghosts, identified as "XX-event" in Figure 5.

AMPLITUDE CORRECTIONS

Field recordings of seismic data as well as physical model data do not directly indicate target reflection coefficients due to numerous factors. The most important factors that disturb seismic amplitudes are geometrical spreading, transmission loss, anelastic attenuation, interference of primary and ghost reflections due to a free surface, interbed multiples, and source/receiver array response (e.g., Spratt et al., 1993). Such effects alter amplitudes and are independent of the model properties and should be compensated for so that the reflection amplitudes represent the reflection coefficients of an interface.

Duren (1992) presented AVO corrections on marine data to reveal amplitude behavior with offset. We follow Duren (1992) and apply a deterministic amplitude correction for our physical model reflection amplitudes. As previously explained, our experimental design avoids overlapping primary and ghost events, and the interference of interbred multiples with our target event. Assuming homogeneity of our model layers (ignoring anelastic attenuation), the effects of geometrical spreading, emergence angle, transmission loss, and source/receiver array (which is called source/reciever directivity here) are the relevant factors for our physical model reflection amplitudes.

For a horizontally layered medium as shown in Figure 7, the recorded vertical-component

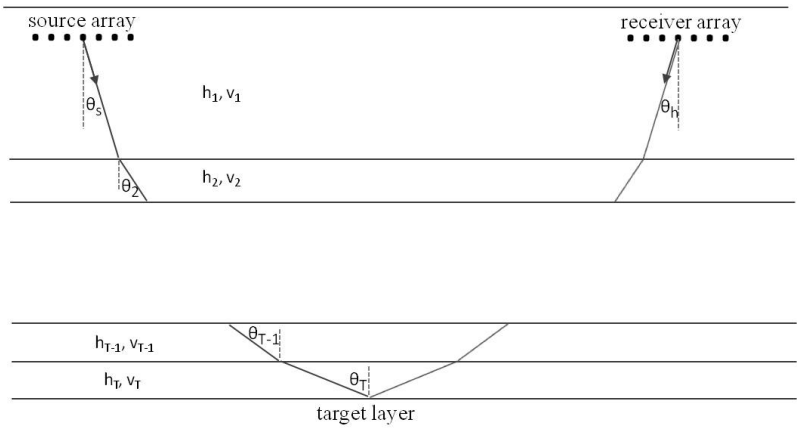

FIG. 7. Raypath geometry for horizontally layered subsurface (after Duren (1991)).

reflection amplitude (along a CMP profile at azimuth ϕ) can be considered as

$$A(x,f) = \frac{SD(\theta_s,f)D(\theta_h,f)L(x)\cos\theta_h}{D_g(x)}R_T(\theta_T) \tag{1}$$

where f is the frequency, x is the source-receiver offset, θ_s is the source radiated ray direction, θ_h is the emergence angle at the receiver, θ_T is the incident angle at the target reflector, and

$$\begin{aligned} A(x,f) &= \text{vertical-component recorded reflection amplitude,} \\ S &= \text{overall scalar related to source strength,} \\ D(\theta_s,f) &= \text{source directivity along } \theta_s \text{ direction,} \\ D(\theta_h,f) &= \text{receiver directivity along } \theta_h \text{ direction,} \\ R_T(\theta_T) &= \text{target's reflection coefficient,} \\ D_g(x) &= \text{geometrical spreading,} \\ L(x) &= \text{transmission loss.} \end{aligned}$$

Each of the factors in equation 1 should be compensated for so that the physical model reflection amplitude, $A(x,f)$, after corrections, estimates the reflection coefficient, $R_T(\theta_T)$. Assuming a horizontally stratified subsurface and ray theory the subsurface factors in equation 1 can be estimated. For a given offset and target depth, we have traced the primary's raypath employing Snell's law, using a PP ray-tracing function from the CREWES MatLab library, to determine the ray incident angle at the target reflector, the emergence angle at the receiver location, the geometrical spreading, and transmission loss. Appendix C presents the corrections for these subsurface factors in greater detail. In the next, the directivity correction for physical model transducers, $D(\theta,f)$, is presented.

Source/receiver directivity

Single sources and receivers in the field are generally very small compared to seismic wavelengths and are treated as point sources and receivers. The physical model transducers,

with their larger dimensions, cannot be treated as point sources/receivers. They produce the seismic wavefield where amplitudes are directionally biased. An illustration of the produced pressure field is shown in Figure 8, less energy propagates at high angles (i.e., far offsets). The directionality behavior of physical model transducers can be best described by a seismic array. It is well known that the radiated wavefield from a source array has a directivity pattern. (Parkes et al., 1984; Duren, 1988). Directivity is defined as the ratio of radiated energy density in a particular direction to the average radiated energy (Duren, 1988). Next, we numerically model the dircetivity of a circular source transducer.

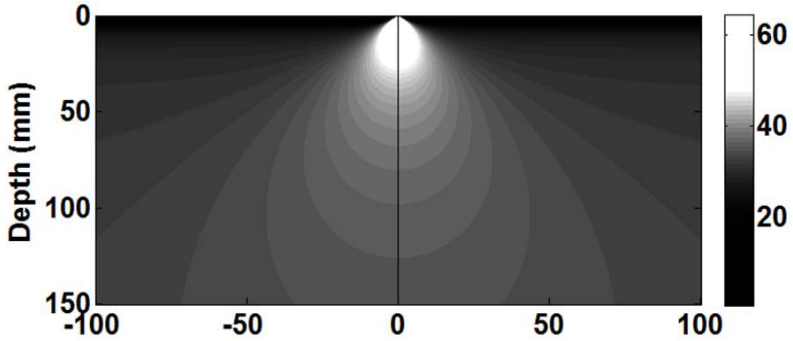

FIG. 8. The calculated pressure field for a circular transducer of a diameter of 12mm as a function of depth and angle for a frequency of 200 kHZ (after Buddensiek et al. (2009)).

Consider a source transducer. Assuming Huygens's principle, it can be regarded as an array of point sources where each individual element radiates the same waveform simultaneously with the others. Take a coordinate system with the origin at the center of the source transducer, and the circular planar transducer in the $z = 0$ plane with the individual element location at $\vec{r_s} = (x_s, y_s, 0)$, and a point receiver in the (x, z) plane at $\vec{r} = (R\cos\theta, 0, R\sin\theta)$ (Figure 9). Consider a monochromatic acoustic wavefield radiated from individual points in the transducer and detected at the point receiver, described by the Helmholtz Green function

$$p_0 \frac{e^{ik|\vec{r}-\vec{r_s}|}}{|\vec{r}-\vec{r_s}|}. \tag{2}$$

Here p_0 is the initial pressure, $k = 2\pi/\lambda$ is the spatial wavenumber, and $\vec{r_s}$ is the location of the point source. The total far-field is the sum of individually radiated wavefields

$$P(\vec{r}, f) = p_0 \int_{-a}^{a}\int_{-a}^{a} \frac{e^{ik|\vec{r}-\vec{r_s}|}}{|\vec{r}-\vec{r_s}|} dx_s dy_s, \tag{3}$$

where $P(\vec{r}, f)$ is the pressure field, and a is the transducer radius. When $\vec{r}$ is much greater than the transducer radius, equation 3 is described analytically (e.g., Schmerr, 1998; Kundu, 2003) by:

$$\begin{aligned} P(\vec{r}, f) &= p_0 \frac{e^{ikR}}{R}\frac{J_1(X)}{X}, \\ X &= \frac{\pi(2a)f}{v}\sin\theta, \end{aligned} \tag{4}$$

where J_1 is the Bessel function of order 1 and v is the P-wave velocity. In this equation, the e^{ikR}/R term is the wavefield generated by a point source at the center of the transducer as

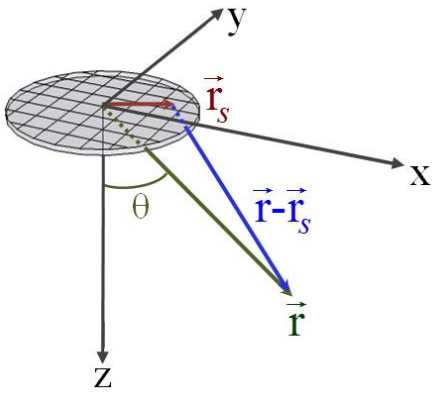

FIG. 9. A circular source transducer in the $z = 0$ plane as source array, with the point receiver at location $\vec{r}$.

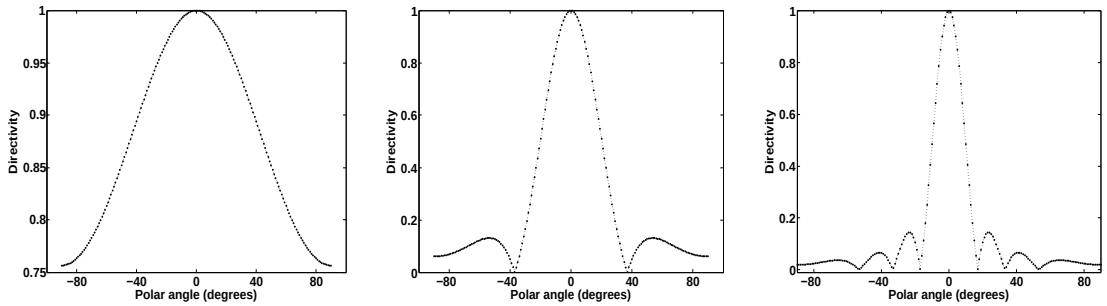

FIG. 10. Directivity of a circular transducer with the diameter of (a) 1.3mm, (b) 6.0mm, (c) 12mm, for a frequency of 500kHz.

detected at a point receiver at a distance R. The second term defines the directivity of the circular transducer assuming unit average energy. Hence, the directivity of the transducer is

$$D(\theta, f) = \frac{J_1(X)}{X}. \tag{5}$$

Figure 10 shows the dircetivity function for three transducer sizes. Our transducers, with a diameter of 1.27mm have a directivity similar to Figure 10(a). The directivity equation for circular transducers is similar to the response of a linear array of length L given by

$$\frac{\sin(\frac{\pi L f}{v}\sin\theta)}{\frac{\pi L f}{v}\sin\theta}. \tag{6}$$

We used equation 5 to compensate for the directivity effect of our source/reciever transducers. By reciprocity, the directional characteristic of a circular transducer is the same whether used as a source or a receiver.

AVO RESPONSE OF THE ISOTROPIC/ISOTROPIC INTERFACE

We corrected the plexiglas top amplitudes for all the effects included in equation 1. In the dircetivity correction, equation 5, for the diameter of the transducers, we followed Bud-

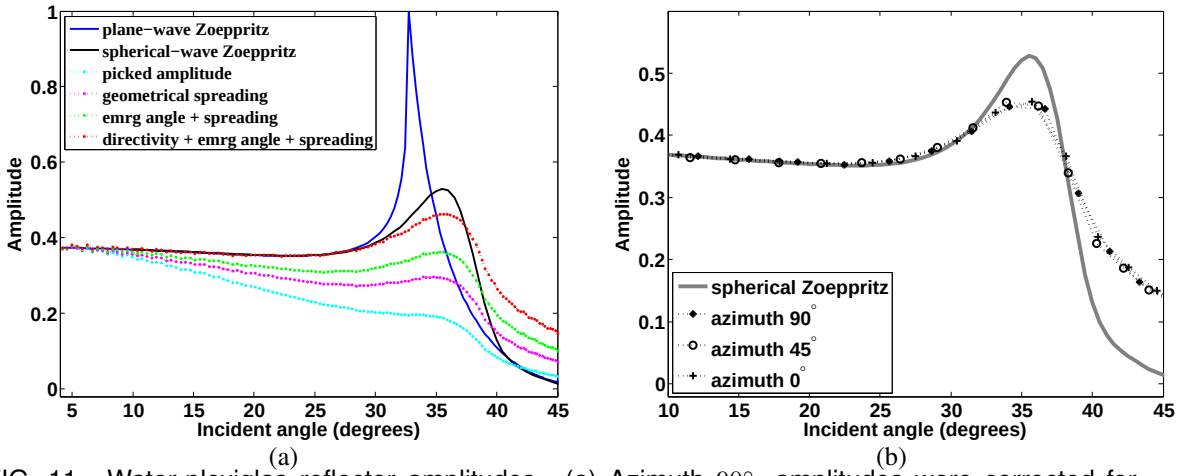

FIG. 11. Water-plexiglas reflector amplitudes. (a) Azimuth $90°$, amplitudes were corrected for geometrical spreading, emergence angle, and directivity effects. (b) Three azimuths.

densiek et al. (2009) and took the value that gives the best match to the observed amplitudes. An effective diameter of 1.4mm was used for our corrections. We compare the corrected amplitudes reflected from the plexiglas top with the plane-wave and spherical-wave reflection coefficients computed with the Zoeppritz equation. The spherical-wave Zoeppritz equation implemented as a JAVA applet by Ursenbach et al. (2006), is available from the CREWES website. The picked raw and corrected amplitudes, along the $90°$ azimuth line, after each correction, are plotted in Figure 11(a) as a function of the incident angle. The picked and corrected amplitudes are calibrated to the theoretical near-offset reflection coefficient, so that the amplitude variations between near and far offset after each correction are revealed. The substantial improvement after each correction indicates the importance of each correction in preparing the amplitude data for an AVO analysis. Figure 11(b) displays the corrected amplitudes reflected from the plexiglas top for three selected azimuths. No azimuthal variations for the plexiglas top, from the interface of the two isotropic media, were observed.

The corrected plexiglas top amplitudes agree very well with the plane-wave solutions for moderate angles of incident, well before the critically refracted arrivals are starting to appear. However, a large discrepancy occurs at far offsets close to the critical angle. The corrected amplitudes follow the spherical-wave predicted amplitudes, with better agreement at incident angles closer to the critical angle, similar to that reported by Winterstein and Hanten (1985); Haase and Ursenbach (2007); Alhussain et al. (2008). However, a perfect agreement, between the observed amplitudes and the spherical-wave predicted amplitudes, is not observed either. We believe this is mostly due to the plane-wave nature of the applied corrections which are based on the assumption of relating the amplitudes to a single ray. However, the reflection of the spherical-waves involves reflections of not just the one by the specular ray but is due to the bunch of rays within the ray beam abound the central ray (Bleistein et al., 2001).

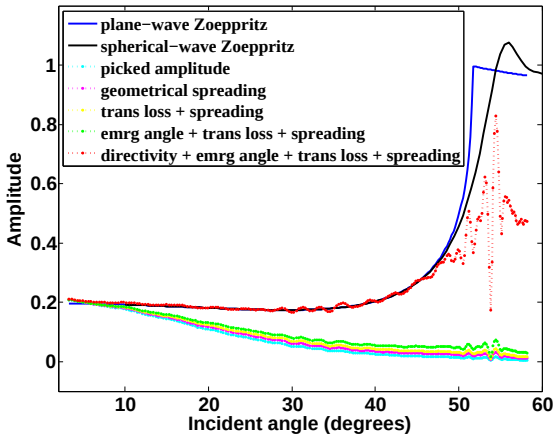

FIG. 12. Fracture top reflector amplitudes, for azimuth $90°$, compared to theoretical reflection coefficient predicted by the Zoeppritz equation.

AZIMUTHAL AVO FROM THE ISOTROPIC/ANISOTROPIC INTERFACE

For the fracture top reflector, we also compare the corrected amplitudes from $90°$ azimuth (the direction of isotropic plane of the fractured layer) with the theoretical reflection coefficients. The picked and corrected amplitudes, after each correction, are plotted in Figure 12. Similar to the plexiglas top reflector, the fracture top reflection amplitudes follow closely the isotropic spherical Zoeppritz predictions.

The corrected amplitude of the fracture top reflector for nine azimuths between $0°$ and $90°$ are shown in Figure 13(a). The corrected amplitudes from only $0°$, $45°$, and $90°$ azimuths are shown in Figure 13(b). The azimuthal amplitude variation, although small, is seen clearly. Note that the AVA variation is small for incident angles before $30°$.

The amplitudes reflected from the top of the fractured layer follow the theoretically predicted reflectivity of Rüger's equation closely for incident angles up to the critical angle (around $53°$), see Figure 14. Reflectivity amplitudes predicted by Rüger's equation are calculated using the elastic properties of plexiglas and the phenolic layer (Table 1). Beyond about $50°$, the deviations of the experimental data from Rüger's prediction are due to the fact that Rüger's equation is valid only for plane waves. The corrected amplitudes reflected from the top of the fractured medium will be used as input to an AVAZ analysis to estimate Thomsen anisotropy parameters of the fractured layer. The AVAZ inversion is presented elsewhere.

Discussions

A piezoelectric transducer produces a wavelet with a restricted bandwidth around its resonance frequency (Buddensiek et al., 2009). Figure 15 shows the amplitude spectrum of one of our physical model seismic traces acquired with the transducers tip are just slightly inside the water. It displays the restricted bandwidth and the strong amplitude at the scaled resonance frequency of 50Hz, while the notches in the amplitude spectrum are caused by ghosts events. In the case of using physical model data in a frequency sensitive inversion, in particular when the low-frequency content is important, such restricted band width

should be considered. Nevertheless, such restricted bandwidth does not affect our amplitude analysis. Another characteristic of a piezoelectric transducer is the change of the

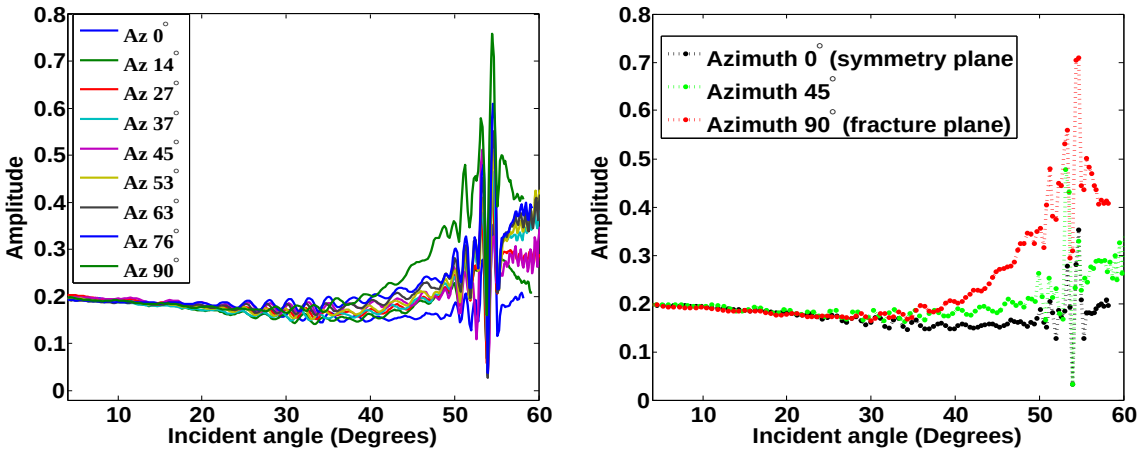

FIG. 13. Fracture top corrected reflection amplitudes from (a) all nine azimuths, (b) only three azimuths.

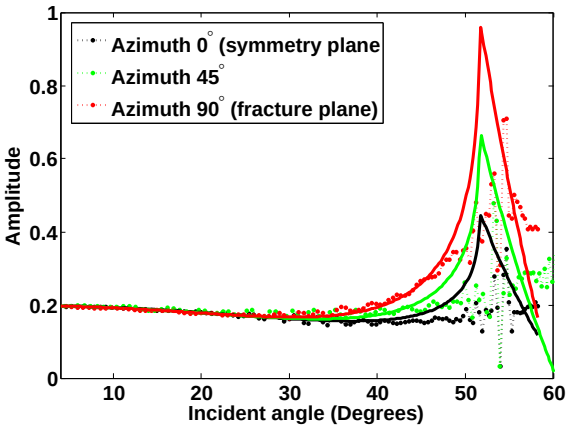

FIG. 14. Fracture top reflector corrected amplitudes from three azimuths (shown by dots), compared to theoretical reflection coefficients predicted by Rüger's equation (shown by solid lines).

radiated waveform with offset (Buddensiek et al., 2009), which is due to the large size of the transducer. In this regard, we finite-difference modeled a seismic wavefront generated by a circular transducer (12mm in size), with the dominant frequency of 500kHz and propagating at a velocity of 3500m/s (Figure 16). The change in wavelet shape from near to far offsets is quite pronounced. The modeling was done using a source array of a length of 12mm, recorded by point receivers, and a seismic wavelength of $7mm$. Nevertheless, for our amplitude analysis, this effect can also be neglected as the size of our source/reciever (1.3mm) is smaller than the emitted wavelength (acoustic wavelength of 2.8mm). Additionally, our data do not show a noticeable change in the wavelet shape between near and far offset traces.

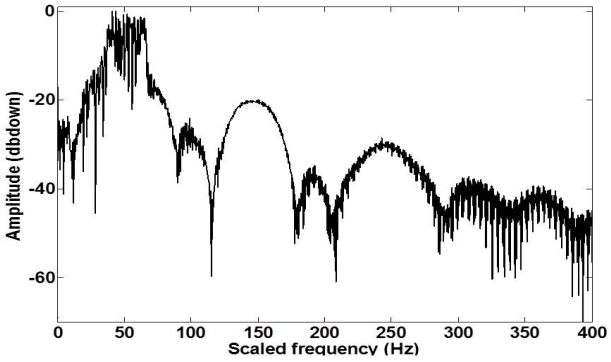

FIG. 15. Amplitude spectrum of one of our physical model traces.

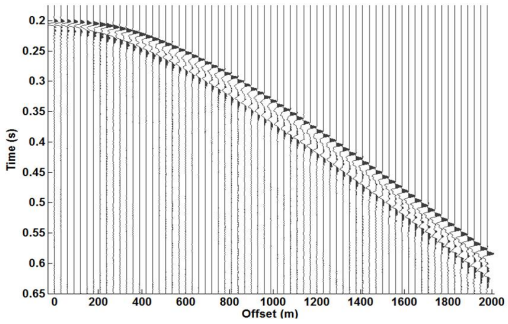

FIG. 16. Finite-difference modeling of a seismic wavefront generated by a 12mm transdcuer.

CONCLUSIONS

We verified the suitability of physical model seismic data for a quantitative amplitude analysis. The reflection amplitudes from isotropic/isotropic and isotropic/anisotropic interfaces are subjected to corrections to make them represent reflection coefficients, and therefore can be used in an AVO analysis. The azimuthal AVO was clearly observed from the amplitudes reflected from the top of a simulated fractured layer, and agreed with theoretical amplitudes.

In physical modeling, real wave propagation occurs, so that the physical model seismic data can be treated as field data. While the traveltimes in physical modeling are reliable, the large, highly-directional transducers disturb the seismic amplitudes, and their effect should be compensated for before any amplitude analysis. We mitigated the directional amplitude responses of the transducers using an array-type (directivity) correction.

APPENDIX A
First source-receiver offset determination

In this appendix, a method to estimate the first source-receiver offset for a physical model data is presented. In a shot gather, consider the first-arrival traveltimes, a linear event propagating with the first-layer P-wave velocity, as

$$ax + b = t, \tag{7}$$

where t are the first-arrival traveltimes, and x is the receiver location. The constant a can be interpreted as the slowness of the first-layer, and $-b/a$ is the first source-receiver offset. The constants a and b can be obtained from the least-square fitting of the first-arrival traveltimes. Using equation 7, the (x, t) picks of the first-arrival event can be used in a linear system of equations,

$$\begin{pmatrix} x_1 & 1 \\ \vdots & \\ x_n & 1 \end{pmatrix} \begin{pmatrix} a \\ b \end{pmatrix} = \begin{pmatrix} t_1 \\ \vdots \\ t_n \end{pmatrix} \tag{8}$$

in which n is the number of the picks. A least-squares solution of system of equation 8 gives an estimate of the first layer velocity and first source-receiver offset.

APPENDIX B
Single-leg ghost event

Here we examine the traveltime of a single-leg ghost event generated due to a free-surface. We prove that a single-leg ghost has the same reflection traveltime as of a wave generated and recorded at the water contact with the transducers.

Assume a virtual wave propagation in which the wave is generated and recorded at water contact with the source and receiver transducers (see Figure 17(a)). The traveltime of this event is

$$tt = \frac{2\sqrt{\frac{x^2}{4} + d^2}}{V_w}, \tag{9}$$

where x is the source-receiver offset, V_w is the P-velocity of water, and d is the reflector depth. With the source-receiver offset written as $x/2 = d\tan\theta$, where θ is the incident angle at the CMP between the source and receiver, equation 9 becomes

$$\begin{aligned} tt &= \frac{2\sqrt{d^2\tan^2\theta + d^2}}{V_w}, \\ tt &= \frac{2d}{V_w\cos\theta}. \end{aligned} \tag{10}$$

Now assume a single-leg ghost at the receiver, see Figure 17(b). With the notation used in Figure 17(b), we have $x/2 = x_1 + x_2,\ x_1 = d_1\tan\theta_a$, $x_2 = d_2\tan\theta_a$ and $d = d_1 + d_2$. Let's call the traveltime related to this single-leg ghost as t_a, then

$$\begin{aligned} t_a &= \frac{2\sqrt{x_1^2 + d_1^2}}{V_w} + \frac{2\sqrt{x_2^2 + d_2^2}}{V_w}, \\ t_a &= \frac{2d_1}{V_w\cos\theta} + \frac{2d_2}{V_w\cos\theta}, \\ t_a &= \frac{2(d_1 + d_2)}{V_w\cos\theta}, \\ t_a &= \frac{2d}{V_w\cos\theta}. \end{aligned} \tag{11}$$

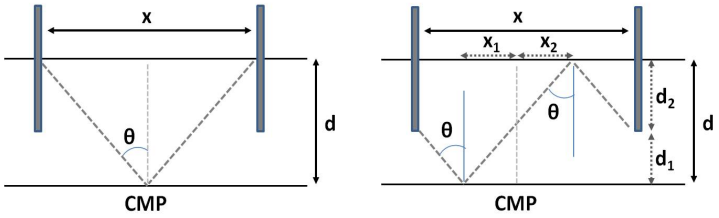

(a) (b)

FIG. 17. (a) Raypath of the virtual wave propagation in which the wave is generated and recorded at water contact. (b) Raypath of a single-leg ghost.

Comparing equation 11 with equation 10 show that $tt = t_a$, which means the traveltime of the single-leg ghost event is equal to the traveltime of a wave generated and recorded at the water contact with the transducers. Therefore, the single-leg ghost event has a constant traveltime independent of the source and receiver transducers' tip depth within the water.

APPENDIX C
AVO corrections for subsurface factors

Some details about the AVO corrections for subsurface effects are presented in this appendix.

Geometrical spreading

For horizontal homogeneous layers, assuming straight raypaths in each layer, for a given offset and target depth, using the velocity model of the overburden layers, the ray tracing function calculates the geometrical spreading factor as (Červený and Ravindra, 1971)

$$D_g(x) = \frac{\cos\theta_s}{v_s}\sqrt{\left(\sum_{j=1}^{k}\frac{h_j v_j}{\cos\theta_j}\right)\left(\sum_{j=1}^{k}\frac{h_j v_j}{\cos^3\theta_j}\right)} \tag{12}$$

where h_j, v_j are the thickness and velocity of the layer containing to the j^{th} ray segment, and θ_j is the angle the j^{th} ray segment makes with the vertical axis. This provides the exact geometrical spreading correction ($D_g(x)$ in equation 1) for horizontal layering which is applied to our physical model reflection amplitudes.

For field data, which lacks details about the overburden layers, such an exact geometrical spreading correction is often not possible. However, there are readily applied zero-offset and offset-dependent geometrical spreading corrections that can be applied to shot gather (or CMP gather) data before move-out is applied. The zero-offset geometrical correction is (Newman, 1973; Resnik, 1993)

$$g_0(t) = V_{rms}^2(t_0)t, \tag{13}$$

where t is two way traveltime and V_{rms} is an estimate of the root-mean-square (rms) velocity at the corresponding zero-offset time, t_0. A single velocity function is used for the entire gather. This provides a good approximate correction, but does not fully compensate for spreading effect at far offsets. An offset-dependent geometrical spreading correction

given by Ursin (1990) is

$$g_1^2(t,x) = g_0^2(t) + \left[2\left(\frac{V_{rms}}{V_1}\right)^2 - 1\right] x^2 + \frac{1}{{t_0}^2}\left(\frac{1}{V_1^2} - \frac{1}{V_{rms}^2}\right) x^4, \tag{14}$$

where x is source-receiver offset, and V_1 is the first layer velocity. Figure 18 shows the water-plexiglas reflector amplitudes versus incident angle that have been corrected for geometrical spreading using corrections by raytracing, zero-offset, and offset-dependent geometrical spreading. The offset-dependent correction compensates nearly as well as the exact raytracing geometrical spreading correction.

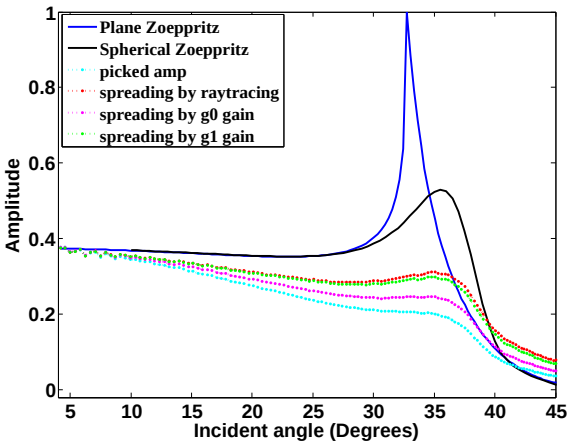

FIG. 18. Geometrical spreading corrections (raytracing, zero-offset, and offset-dependent) applied to the water-plexiglas reflection amplitudes. The amplitudes have been compared to Zoeppritz predicated reflection coefficients.

Transmission loss

Zoeppritz equations can provide the downgoing PP transmission coefficient, $T_{j,j+1}(\theta_j)$, and upgoing PP transmission coefficient, $T_{j+1,j}(\theta_{j+1})$, between layer j and $j+1$. The decrease in amplitude associated with transmission loss between layer j and $j+1$ is the product $T_{j,j+1}(\theta_j) \times T_{j+1,j}(\theta_{j+1})$. The transmission loss factor, $L(x)$ in equation 1, is the total loss for all interfaces along the entire raypath (e.g. Duren, 1991; Spratt et al., 1993):

$$L(x) = \prod_{j=1}^{k-1} T_{j,j+1}(\theta_j) T_{j+1,j}(\theta_{j+1}). \tag{15}$$

For field data, a deterministic correction of transmission loss is problematic as the overburden can not be perfectly characterized. Transmission loss is the most significant problem encountered in AVO analysis (Gassaway, 1984). In practice the transmission loss is compensated for using statistical corrections.

Emergence angle

For vertical component data, the recordings should be converted to total motion for amplitude data to represent reflection coefficients. Knowing the emergence angle (θ_h) at

the receiver location, $\cos(\theta_h)$ factor provides the total motion and is called emergence angle correction in this study.

Scalar factor

After applying all subsurface and surface corrections, a constant scalar factor is required to normalized the amplitude magnitude to the range of $[-1, 1]$, the reflection coefficient range. This scalar factor is the S term in equation 1. The single scalar factor is applied to the entire seismic gather and is related mostly to the source strength and some possible power filters applied in processing.

For a single reflector, the scalar factor can be determined by calibrating the near-offset amplitudes to the normal incident reflection coefficient from the Zoeppritz equations. For a target time window of a seismic gather, the scalar factor can be obtained by minimizing $A(x_0, t) - SR(t)$ in a least-squares sense, where $A(x_0, t)$ are the near-offset amplitudes and $R(t)$ is the reflectivity model defined by well logs or a velocity model. Minimizing

$$b = \sum_{k=1}^{\max} (A_k - SR_k)^2 = \min, \tag{16}$$

means

$$\frac{\partial b}{\partial S} = \sum_{k} -2R_k (A_k - SR_k) = 0, \tag{17}$$

and the scalar becomes (Margrave, 2000):

$$S = \frac{\sum_k R_k A_k}{\sum_k R_k R_k}, \tag{18}$$

where $\sum_k R_k A_k$ is the zero-lag cross-correlation of $R(t)$ and $A(t)$, and $\sum_k R_k R_k$ is the zero-lag autocorrelation of $R(t)$.

ACKNOWLEDGMENT

We thank the sponsors of CREWES for their financial support. Dr P.F. Daley is greatly appreciated for his guidance and editing of the manuscript. Dr Kris Innanen is appreciated for his suggestions to improve the work. Faranak Mahmoudian wishes to thank specially Mahdi Almutlaq and Sayeh Moayerian.

REFERENCES

Alhussain, M., Gurevich, B., and Urosevic, M., 2008, Experimental verification pf spherical-wave effect on the avo responce and implications for three-term inversion: Geophysics, **73**, No. 2, C7–C12.

Bleistein, N., Cohen, J. K., and Stockwell, J. W. J., 2001, Methematics of Multidemensional Seismic Imagning, Migration, and Inversion: Springer.

Bretaudeau, F., Leparoux, D., Durand, O., and Abraham, O., 2011, Small-scale modeling of onshore seismic experiment: A tool to validate numerical modeling and seismic imaging methods: Geophysics, **76**, No. 5, T101–T112.

Buddensiek, M. L., Krawczyk, C. M., Kukowski, N., and Oncken, O., 2009, Performance of piezoelectric transducres in terms of amplitude and waveform: Geophysics, **74**, No. 2, T33–T45.

Chang, C., and Gardner, G. H. F., 1997, Effects of vertically alighned subsurface fractured on seismic reflections: A physical model study: Geophysics, **62**, 245–252.

Cheadle, S. P., Brown, R. J., and Lawton, D. C., 1991, Orthorhombic anisotropy:a physical seismic modeling study: Geophysics, **56**, 1603–1613.

Duren, R. E., 1988, A theory for marine source arrays: Geophysics, **53**, No. 5, 650–658.

Duren, R. E., 1991, Seismic range equation: Geophysics, **56**, No. 7, 1015–1026.

Duren, R. E., 1992, Seismic range equation: Geophysics, **57**, No. 9, 1203–1208.

Gassaway, G. S., 1984, Effects of shallow reflectors on amplitude versus offset (seismic lithology) analysis: SEG expanded abstract, 665–669.

Haase, A. B., and Ursenbach, C. P., 2007, Spherical-wave computational avo modeling in elastic and anelastic isotropic two-layer medis: EAGE Expanded Abstracts.

Krautkrämer, J., and Krautkrämer, H., 1986, Werkstoffprüfung mit Ultrascall:

Kundu, T., 2003, Ultrasonic nondeconstructve evaluation: engineering and biological material characterization: CRC Press.

Luo, M., and Evan, B. J., 2004, An amplitude-based multiazimuth approch to mapping frcatures using p-wave seimsic data: Geophysics, **69**, No. 3, 690–698.

Mah, M., and Schmitt, D. R., 2001a, Experimental determination of the elastic coefficients of an orthorhombic material: Geophysics, **66**, 1217–1225.

Mah, M., and Schmitt, D. R., 2001b, Near point-source longitudinal and transverse mode ultrasonic arrays for material characterization: IEEE, **48**, 691–698.

Mahmoudian, F., Margrave, G. F., Daley, P. F., and Wong, J., 2012, Anisotropy estimation for a simulated fractured medium using traveltime inversion: A physical modeling study: SEG Expanded Abstract.

Margrave, G. F., 2000, Methods of seismic data processing: University of Calgary course notes.

Newman, P., 1973, Divergence effects in a layered earth: Geophysics, **38**, 481–488.

Parkes, G. E., Hatton, A., and Haugland, T., 1984, Marine source array directivity, a new wide airgun array system: First Break, **2**, No. 4, 4–15.

Resnik, J. R., 1993, Seismic data processing for avo and ava analysis: Investigation In Geophysics Series, , No. 8, 175–189.

Rüger, A., 2001, Reflection coefficients and azimuthal AVO analysis in anisotropic media: Goephysical Monograph Series.

Schmerr, L. W., 1998, Fundamentals of nondeconstructve evaluation - A modeling approach: Plenum Press.

Spratt, R. S., Goins, N. R., and Fitch, T. J., 1993, Pseudo-shear - the analysis of avo: Investigation In Geophysics Series, **8**, 37–56.

Tadepalli, S. V., 1995, 3-d avo analysis: Physical modeling study: PhD. Thesis, University of Houston.

Ursenbach, C. P., Hass, A. B., and Downton, J. E., 2006, Improved modeling of spherical-wave avo: CREWES Research Reports.

Ursin, B., 1990, Offset-dependent geometrical spreading in a layered medium: Geophysics, **55**, No. 4, 492–496.

Červený, V., and Ravindra, R., 1971, Theory of seismic head waves: University of Toronto Press.

Wang, S., and Li, X., 2003, Fracture detection using 3d seismic data: A physical modeling study: SEG Expanded Abstracts.

Winterstein, D. F., and Hanten, J. B., 1985, Suppercretical reflections observed in p- and s-wave data: Geophysics, **50**, 185–195.

Wong, J., Hall, K. W., Gallant, E. V., Maier, R., Bertram, M., and Lawton, D. C., 2009, Seismic physical modeling at university of calgary: CSEG recorder.